Nanoscale

Accepted Manuscript

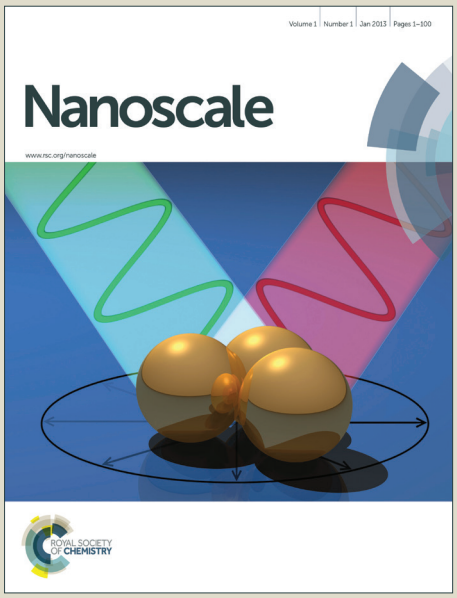

Journal Name RSCPublishing

ARTICLE

Cite this: DOI: 10.1039/x0xx00000x

Received 00th January 2012,
Accepted 00th January 2012

DOI: 10.1039/x0xx00000x

www.rsc.org/

High-Efficiency Synergistic Conversion of CO_2 to Methanol Using Fe_2O_3 Nanotubes Modified with Double-Layer Cu_2O Spheres

Peiqiang Li*, Hua Jing, Jinfeng Xu, Chenxiao Wu, Hui Peng, Jing Lu, Fusui Lu*

Cuprous oxide/hematite nanotubes (Cu_2O/Fe_2O_3NTs) were prepared by the potentiostatic electrodeposited method in which different structured Cu_2O materials were modified onto Fe_2O_3 NTs surface. Among them, the material with double-layer Cu_2O spheres (Cu_2O/Fe_2O_3 NTs-30) showed excellent photoelectrocatalytic (PEC) properties with a suitable energy band gap (1.96 eV) and smaller overpotential (0.18 V). Furthermore, Cu_2O/Fe_2O_3 NTs-30 showed two types of synergism in the PEC reduction of CO_2: (i) between electrocatalysis and photocatalysis and (ii) between Cu_2O and Fe_2O_3NTs. The faradaic efficiency and methanol yield reached 93% and 4.94 mmol L^{-1} cm^{-2} after 6 h, respectively.

Introduction

Carbon dioxide (CO_2) released by burning fossil fuels is a primary cause of global warming; therefore, the capture and efficient use of CO_2 have become an important issue. Among all the possible solutions, the catalytic conversion CO_2 to hydrocarbon fuels is a crucial goal that may positively influence the global carbon balance. Recently, attempts have been made to utilize CO_2 as a natural resource, i.e., as a feedstock rather than a waste product requiring costly disposal, such as high temperature and high pressure[1,2]. The photocatalytic (PC) reduction CO_2 proceeds under ambient temperature and pressure driven by solar energy, which is inexhaustible in supply and always available for use[3-5]. However, the PC conversion efficiency of CO_2 to methanol (CH_3OH) and other energy-rich compounds is generally low. One of the reasons is the low utilization of visible light caused by the width of the energy band gap of the semiconductor material unsuitable for this purpose.

Moreover, electrocatalytic (EC) function has also received extensive attention in the field of CO_2 reduction because of the possibility of applying renewable electrical energy as the driving force. Furthermore, EC function is also conducted under ambient temperature and pressure which can dramatically simplify and lower the cost of CO_2 conversion to fuel[6-10]. An efficient catalyst should mediate the transfer of multiple electrons and protons to CO_2 at low overpotential, reduce CO_2 in the presence of H_2O, and selectively afford one product. However, the EC reduction CO_2 suffers from one or more of the following problems: low energetic efficiency (i.e., large overpotential requirement), rapid loss of CO_2 reduction activity in favor of H_2O reduction, and poor selectivity[11,12].

To achieve a more efficient catalytic process, photoelectrocatalytic (PEC) processes have been studied using visible light-sensitive materials to convert CO_2 to small-molecule organic fuels[13-17]. The first use of a photocatalyst, as a photocathode, for the PEC reduction CO_2 was reported over 30 years ago[13]. Most of the researches about the PEC reduction of CO_2 involve electrically assisted photocatalysis[14-16]. A small bias is added to the catalyst materials based on the PC reduction to effectively separate the photo-generated holes and electrons and achieved higher photoelectric conversion efficiency; however, the applied bias is too small to conduct the EC reduction independently. Previously, we reported photo-enhanced electrocatalysis[17], with efficient reduction efficiency. However, the light itself could not provide the desired PC function independently. Therefore, we combined EC and PC functions to achieve a synergistic function between them on the same catalytic surface.

To achieve a synergistic function between PC and EC, the selection of a catalyst is the key point, which requires that the catalyst not only matches the energy band for the PC reduction, but also matches the small overpotential for the EC reduction simultaneously. Among the available materials, hematite (Fe_2O_3) is an excellent semiconductor photocatalyst and has been widely investigated because it is environmentally benign, very abundant,

P. Q. Li, H. Jing, J. F. Xu, C. X. Wu, P. Hui, J. Lu, F. S. Lu
Department of Chemistry
Shandong Agricultural University
Shandong 271018, China
Corresponding Author E-mail: chem_carbon@yahoo.cn; pqli@sdau.edu.cn
†Electronic Supplementary Information (ESI) available: Reduction of CO_2 to Low Carbon Alcohols on CuO FCs/Fe_2O_3 NTs Catalyst with Photoelectric Dual Catalytic Interfaces. See DOI: 10.1039/b000000x/

and inexpensive[18-20]. Different hematite-based hierarchical nanoarchitectures have been developed, such as nanowires, flowerlike, urchinlike, nanobelts, nanotubes, nanorods, elliptic superstructures, and dendritic-micropines[21]. Among them, Fe_2O_3 nanotubes (NTs) are extensively used as photocatalyst because of its large surface area, efficient charge transferring capacity, high active sites, and the low recombination of electron-hole pairs[22]. The most important characteristic is that Fe_2O_3 has a narrow band gap (2.2 eV) that can absorb light of wavelength shorter than 600 nm. However, the reduction of Fe_2O_3 is very weak for the positive conduction band (0.28 eV) [23].

To achieve suitable conduction and valence bands for the catalytic reduction of CO_2, cuprous oxide (Cu_2O) was selected to couple with Fe_2O_3 NTs. Cu_2O is a widely used p-type metal-oxide semiconductor, and its conduction band is located at -1.3 eV (vs. normal hydrogen electrode (NHE)) more negative than that of Fe_2O_3[16], resulting in a strong reductive efficiency. In theory, the coupling of Cu_2O to Fe_2O_3 may lead to excellent PC reduction efficiency for CO_2 owing to the matched energy band gap. Moreover, Cu_2O is an outstanding electrocatalyst because of its great selectivity to CH_3OH and excellent conductive ability[24,25]. Therefore, it is expected that the combination of the two materials may exhibit a great PEC performance.

In this study, several Cu_2O/Fe_2O_3 NTs with different morphologies were prepared by the potentiostatic electrodeposition method in which Cu_2O films were deposited onto the surface of Fe_2O_3 NTs at different electrodeposition times. The as-prepared materials were investigated by a series of photochemical and electrochemical measurements, indicating that the Cu_2O/Fe_2O_3 NTs at a deposition time of 30 min showed more excellent PEC properties than the materials obtained at other deposition times. Compared to Cu_2O/Fe or Fe_2O_3 NTs, the Cu_2O/Fe_2O_3NTs showed superior PEC reduction performance for the efficient conversion of CO_2 to CH_3OH. The faradaic efficiency and CH_3OH yield reached 93% and 4.94 mmol L^{-1} cm^{-2} after 6 h, respectively. The Cu_2O/Fe_2O_3NTs material showed two types of synergistic function: (i) between the two materials (Cu_2O and Fe_2O_3) and (ii) between the PC and EC functions. The research provided a new methodology for the material design for the PEC reduction of CO_2; the PEC synergistic conversion of CO_2 has a great environmental and social significance.

Results and Discussion

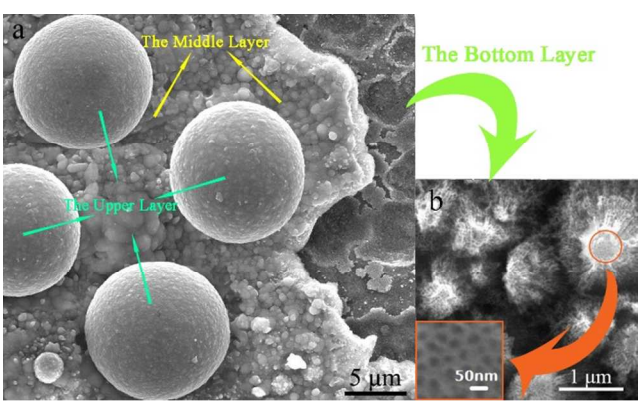

Figure 1. (a), (b) Scanning electron microscope (SEM) images of Cu_2O/Fe_2O_3 NTs at a deposition time of 30 min and Fe_2O_3 NTs. (inset of b: high-magnification SEM image of Figure 1b).

The Cu_2O/Fe_2O_3 NTs were prepared by the simple and practical potentiostatic electrodeposition method. Figure 1a shows the SEM image of the Cu_2O/Fe_2O_3 NTs at a deposition time of 30 min; three layers are clearly observed. The bottom layer is Fe_2O_3 NTs; the amplified Fe_2O_3 NTs grew *in situ* as volcano shape (Figure 1b), which distributed evenly on the surface. The inset of Figure 1b shows that the diameter of Fe_2O_3 NTs is very small (~20 nm). The middle layer in Figure 1a shows spherical Cu_2O evenly distributed with a particle size of 200-500 nm. The upper layer in Figure 1a is evenly distributed, with larger and more regular Cu_2O spheres than the middle one. The diameter of larger Cu_2O spheres is approximately 12 μm. To the best of our knowledge, such a novel three-layer structure is reported for the first time.

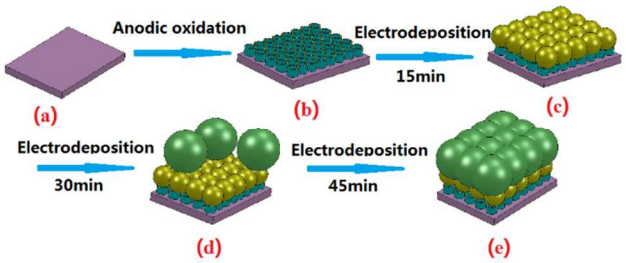

Scheme 1. Growth mechanism of Cu_2O/Fe_2O_3NTs composite.

Scheme 1 shows the growth mechanism of the Cu_2O/Fe_2O_3 NTs, demonstrating the changes in the morphology with the progress in electrodeposition. Herein, Cu_2O/Fe_2O_3 NTs-15, Cu_2O/Fe_2O_3 NTs-30, and Cu_2O/Fe_2O_3 NTs-45 represent the Cu_2O /Fe_2O_3 NTs with the electrodeposition times of 15 min, 30 min, and 45 min, respectively. First, it was a piece of iron, as shown in Scheme 1a. During the electrochemical anodic oxidation treatment, Fe_2O_3 NTs *in situ* grew on the iron plate (Scheme 1b), as shown in Figure 1b. Then, using Fe_2O_3 NTs as the working electrode, potentiostatic electrodeposition was conducted for 15 min, as shown in Scheme 1c. The Cu_2O nanosphere layer was evenly distributed on the surface of the Fe_2O_3 NTs. The scanning electron microscope (SEM) image shows the existence of the Cu_2O nanosphere layer (Figure S1). When the deposition time reached 30 min, as shown in Scheme 1d, bigger Cu_2O spheres appeared and formed another Cu_2O layer, which was sparse and extremely regular. A significant portion of the middle layer was exposed owing to the sparse upper layer (Figure 1a). When the deposition time reached 45 min, the Cu_2O microspheres were significantly produced and distributed in one layer (Scheme 1e), which was thicker than the middle Cu_2O layer and totally covered the other two (Figure S2). Among the three different types of structures, Cu_2O/Fe_2O_3 NTs-30 perhaps showed the largest specific surface that had more active sites for the catalytic reaction.

The best activity of Cu_2O/Fe_2O_3 NTs-30 was proved by the maximum absorption intensity for visible light (MAI-vis), energy band gap (E_g), electrochemical impedance spectroscopy (EIS), and the overpotential of EC reduction of CO_2. As shown in Table 1, in

terms of the photochemical properties, the E_g was obtained after a series of calculations from the UV-visible absorption spectrum[26]. The Cu_2O/Fe_2O_3 NTs-15, Cu_2O/Fe_2O_3 NTs-30, Cu_2O/Fe_2O_3 NTs-45 were found to have similar E_g value (~1.96 eV), indicating that the Cu_2O-loading had no obvious effect on E_g. However, Cu_2O/Fe_2O_3 NTs-30 with the highest value of MAI-vis indicated that the material possessed the highest utilization efficiency for visible light and may possess better PC properties than the others. In terms of electrochemical properties, Cu_2O/Fe_2O_3 NTs-30 had the smallest EIS, indicating that this type of structure possessed the highest electron transfer efficiency, and it may favor the catalytic reduction of CO_2. Furthermore, the lowest overpotential (0.26 V) of Cu_2O/Fe_2O_3 NTs-30 indeed proved that the target material showed the best EC reduction performance for CO_2. In the PEC process, Cu_2O/Fe_2O_3 NTs-30 has the largest CH_3OH yield than the other electrodeposited time. In summary, Cu_2O/Fe_2O_3 NTs-30 exhibited not only the best photochemical performance, but also the best electrochemical performance than the other materials obtained at different deposition times. Therefore, we further studied Cu_2O/Fe_2O_3 NTs-30.

Table 1. Optical and electrical properties of Cu_2O/Fe_2O_3 NTs prepared at different electrodeposition times.

	Photochemical properties		Electrochemical properties		PEC 6 h
	MAI-vis (a.u.)	E_g (eV)	EIS (ohm)	Overpotential (V)	CH_3OH (mmol L^{-1} cm^{-2})
0 min	1.246	2.03	1400.2	0.45	1.29
15 min	0.935	1.97	793.2	0.29	2.35
30 min	1.262	1.96	232.3	0.26	4.94
45 min	1.028	1.96	445.1	0.47	3.09

First, the crystal structures of the as-prepared materials were analyzed by X-ray diffraction (XRD). As shown in the XRD spectra (Figure 2a), the diffraction peaks are strong and sharp, indicating good crystallization[27]. The major strong characteristic peaks of Fe_2O_3 NTs appeared at 2θ of 24.19°, 30.27°, 33.31°, 35.61°, 43.5°, 49.44°, 54.25°, 57.1°, 62.64°, and 65.2°, corresponding to the crystal faces of (012), (206), (104), (110), (113), (024), (116), (112), (214), and (300), respectively. Its lattice parameters of a = 5.0491 Å and c = 13.6577 Å, matched well with JCPDS, No. 33-0664 of standard α-Fe_2O_3 sample, indicating that the sample was indeed α-Fe_2O_3[23]. The major strong characteristic peaks of Cu_2O/Fe_2O_3 NTs-30 and Cu_2O/Fe appeared at 2θ of 36.72°, 43.41°, 61.75°, and 74.33°, corresponding to the crystal faces of (111), (200), (220), and (311), respectively. Its lattice parameters, a = b = c = 4.260 Å, matched well with JCPDS card (No. 65-3288) of Cu_2O[28]. After Cu_2O was loaded on Fe_2O_3 NTs, the peaks of Fe_2O_3 NTs weakened or even disappeared as a result of almost complete coverage of the Cu_2O on the surface of Fe_2O_3 NTs, which also agreed well with the SEM image (Figure 1a).

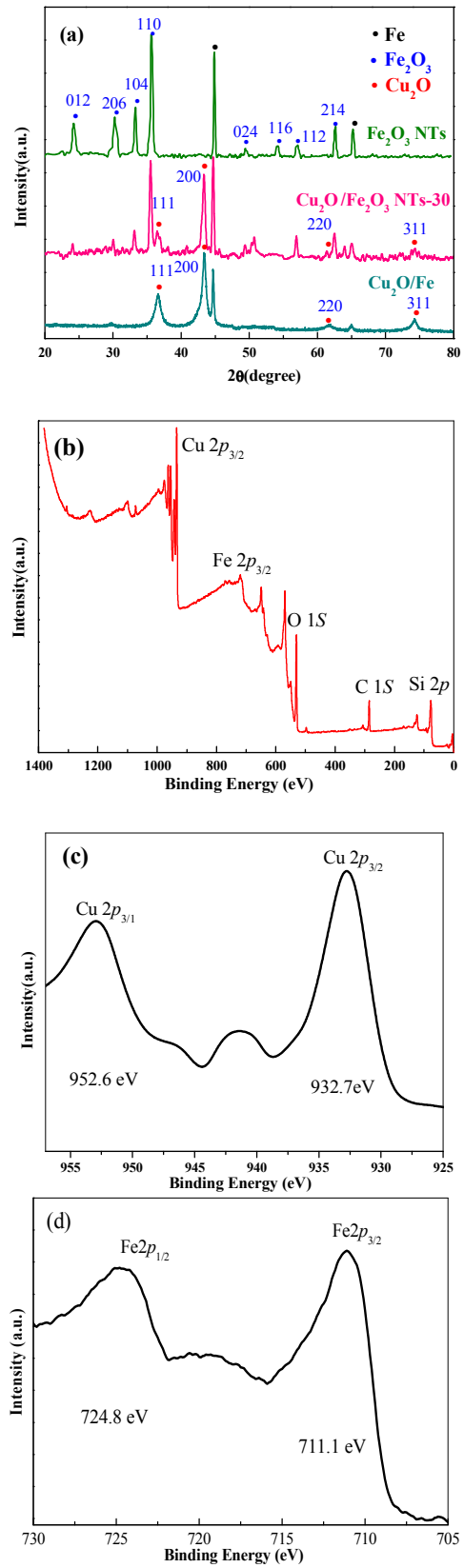

Figure 2. (a) X-ray diffraction spectra of Cu_2O/Fe_2O_3 NTs-30, Cu_2O/Fe, and Fe_2O_3 NTs (blue dot: crystal planes of Fe_2O_3 NTs, black dot: crystal planes of Fe, red dot: crystal planes of Cu_2O), (b) X-ray photoelectron

spectroscopy (XPS) spectrum of Cu_2O/Fe_2O_3 NTs-30 and the corresponding high-resolution XPS spectra of Cu2*p* (c), Fe2*p* (d). NTs = nanotubes.

Figure 2b shows the X-ray photoelectron spectroscopy (XPS) spectrum of Cu_2O/Fe_2O_3 NTs-30, and the data has been revised by C1s (284.6 eV). The wide-scan XPS spectrum showed the predominant presence of C, O, Fe, and Cu elements. Among those elements, O, Cu, and Fe elements were from the as-prepared composites, and the C element was from the XPS instrument itself. Based on the corresponding high-resolution XPS spectra of $Cu2p_{1/3}$ and $Cu2p_{2/3}$, the comparison of the standard XPS spectrum showed that the valence states of the elements prepared were Cu^{+1} (Figure 2c)[29]. The photoelectron peaks of $Fe2p_{3/2}$ and $Fe2p_{1/2}$ appeared ~711.1 eV and 724.8 eV, respectively (Figure 2d), which agreed well with the literature values[30] and indicated the existence of α-Fe_2O_3. Thus, the material was proved to be Cu_2O/Fe_2O_3.

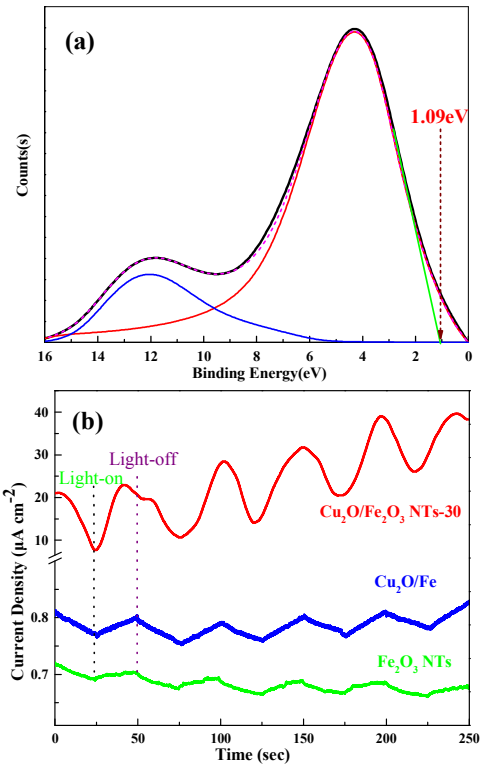

Figure 3. (a) Valence-band photoemission spectrum of Cu_2O/Fe_2O_3 NTs-30, (b) current-time (*i-t*) curve of Cu_2O/Fe_2O_3 NTs-30, Cu_2O/Fe, Fe_2O_3 NTs. The experiment was measured at the open circuit potential in 0.1 mol L^{-1} $KHCO_3$ solution with CO_2 purged and light-on or light-off at every 25 s interval.

Figure 3a shows further analysis of the XPS spectrum. It is the valence-band photoemission spectrum and Gaussian fit graph of Cu_2O/Fe_2O_3 NTs-30 based on the XPS spectrum (Figure 2b). The valence-band maximum (VBM) of the material was directly determined from the electron-emission spectrum by the linear extrapolation of the onset of the valence-band emission[31]. As shown in Figure 3a, the VBM is 1.09 eV. Table 1 showed that the energy band gap of Cu_2O/Fe_2O_3 NTs-30 was narrowed from 2.03 eV to 1.96 eV after modifying Fe_2O_3 NTs with Cu_2O, indicating that Cu_2O/Fe_2O_3 NTs-30 could absorb visible light shorter than 733 nm, and the absorption range for visible light was significantly broadened. Thus, the conduction-band minimum (CBM) could be obtained by the D-value of the VBM and E_g, which was -0.87 eV. This value was more negative than the CO_2/CH_3OH potential (-0.38 V vs. NHE), indicating Cu_2O/Fe_2O_3 NTs-30 with excellent PC reduction ability. Above all, the modification of Fe_2O_3 NTs with Cu_2O greatly improved the material's PC reduction performance in theory because of the narrowed E_g and more negative CBM.

Furthermore, current-time (*i-t*) experiment was used to test the PC performance in practice. The *i-t* curves were measured at the open circuit potential in 0.1 mol L^{-1} $KHCO_3$ solution with CO_2 purged under light on or off conditions. The current density D-value of Cu_2O/Fe_2O_3 NTs-30 between illumination and dark was ~15 μA cm^{-2}, which was obviously larger than those of Cu_2O/Fe (0.051 μA cm^{-2}) and Fe_2O_3 NTs (0.033 μA cm^{-2}). Further, the current density D-value of Cu_2O/Fe_2O_3 NTs-30 was 300 and 450 times those of Cu_2O/Fe and Fe_2O_3 NTs, respectively. Thus, it proved that the coupling of Cu_2O with Fe_2O_3 NTs greatly enhanced the PC reduction of CO_2. In addition, the current density of Fe_2O_3 NTs decreased slightly with time, indicating the occurrence of light corrosion. The current density of Cu_2O/Fe almost had no change, indicating that the Cu_2O had good photochemical stability. Excitingly, after coupling Cu_2O to Fe_2O_3 NTs, the light corrosion stopped. We assumed that Cu_2O protected Fe_2O_3 NTs against the light corrosion and strengthened the PC reduction ability. It was greatly consistent with the former theory.

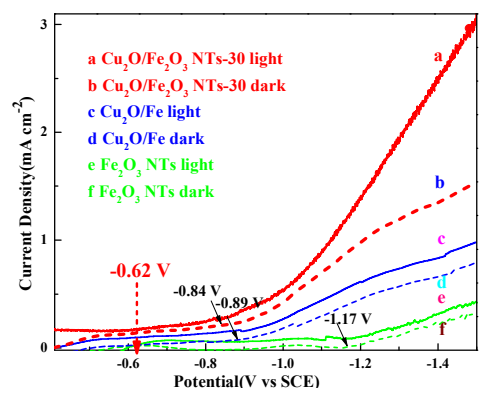

Figure 4. Current-potential (*I'-V*) curves of the three materials under irradiation or dark (the black arrows point to the onset potential of the reduction of CO_2).

The linear-sweep voltammetry (LSV) results of Cu_2O/Fe_2O_3 NTs-30, Cu_2O/Fe, Fe_2O_3 NTs measured under the dark or visible-light irradiation, with N_2 or CO_2 bubbling are shown in Figure 4. The net current density (*I'*) was calculated by subtracting the current density of hydrogen evolution (the current density purged N_2) from the total current density (the current density purged CO_2). The overpotential of the EC reduction CO_2 on Fe_2O_3 NTs was ~550 mV; however, that of Cu_2O/Fe was only 270 mV. After coupling Cu_2O to Fe_2O_3 NTs, the overpotential of the EC reduction CO_2 further decreased to 220 mV. Thus, the Cu_2O modification decreased the overpotential of the EC reduction of CO_2, decreasing the energy consumption in the EC reduction of CO_2. Moreover, the overpotential of Cu_2O/Fe_2O_3 NTs-30 under the irradiation

decreased to 40 mV than the dark condition, indicating that the light irradiation enhanced the material's EC reduction performance. This result agreed well with that reported previously[17].

The -1.3 V (vs. saturated calomel electrode (SCE)) potential was taken as an example, as determined from the following product analysis, for further analysis. It was found that $I'_{Cu2O/Fe2O3\ NTs\text{-}30\text{-}dark}$ was about two times larger than $I'_{Cu2O/Fe\text{-}dark}$ and about ten times larger than $I'_{Fe2O3\ NTs\text{-}dark}$. This result clearly shows that the EC reduction performance of the target material greatly enhanced after introducing Cu_2O onto Fe_2O_3 NTs. In the PEC reduction of CO_2, $I'_{Cu2O/Fe2O3\ NTs\text{-}30\text{-}light}$ was ~1.6 times larger than $I'_{Cu2O/Fe2O3\ NTs\text{-}30\text{-}dark}$, indicating that the EC reduction performance of the target material could be greatly enhanced by the light irradiation. This may lead to the synergistic function between the PC and EC reductions.

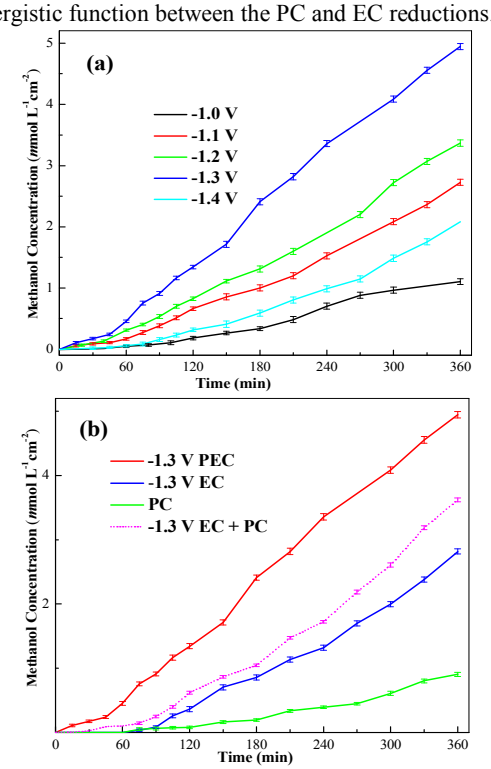

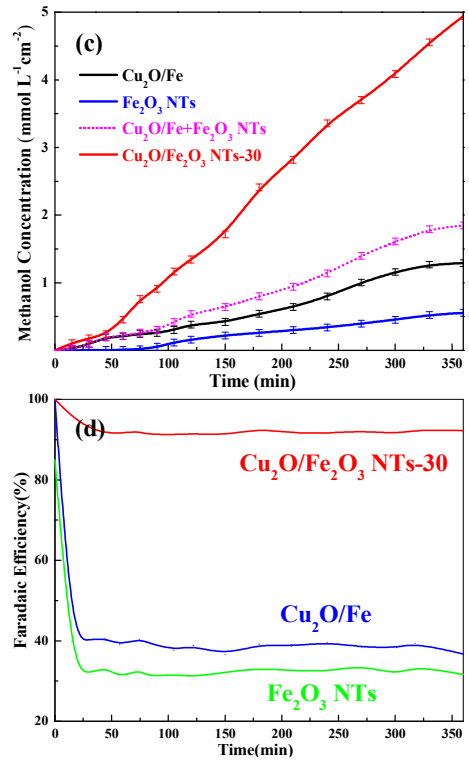

Figure 5. (a) Methanol yield of the PEC reduction of CO_2 on Cu_2O/Fe_2O_3 NTs-30 at different potentials (vs. SCE), (b) Methanol yield of the PEC, PC, and EC reduction of CO_2 on Cu_2O/Fe_2O_3 NTs30, (c) Methanol yield of the PEC reduction CO_2 on Cu_2O/Fe_2O_3 NTs-30, Cu_2O/Fe, and Fe_2O_3 NTs at -1.3 V (vs. SCE), (d) Faradaic efficiency of methanol on Cu_2O/Fe_2O_3 NTs-30, Cu_2O/Fe, and Fe_2O_3 NTs in the PEC process.

The main product of the PEC reduction CO_2 on Cu_2O/Fe_2O_3 NTs-30 was CH_3OH, as tested by GC, and no other products were detected. Further, when the parallel blank experiment (in 0.1 mol L^{-1} $KHCO_3$ solution without CO_2 purging) was conducted, CH_3OH could not be obtained, indicating that the carbon in CH_3OH originated from the injected CO_2. Figure 5a shows that from -1.0 V to -1.3 V (vs. SCE), the CH_3OH yield increased, and from -1.3 V to -1.4 V (vs. SCE) it decreased. The results can be explained as follows: in the range 0-1.3 V, as the potential became more negative, the production quantity of CH_3OH increased gradually because the CO_2 reduction was the main reaction that occurred. When the potential was more negative than -1.3 V, hydrogen evolution becomes the main reaction, and the production quantity of CH_3OH decreased. Further, the highest CH_3OH yield was 4.94 mmol L^{-1} cm^{-2} after 6 h on Cu_2O/Fe_2O_3 NTs-30.

Next, the PEC, PC, and EC reductions of CO_2 on Cu_2O/Fe_2O_3 NTs-30 were compared (Figure 5b); the CH_3OH content reached 4.94, 0.90, and 1.39 mmol L^{-1} cm^{-2}, respectively. From the CH_3OH yield point of view, the EC property of the composite catalyst was better than the PC performance. However, when PC was coupled to EC, a higher yield was obtained, and this value was even higher than that of the simple sum of the EC and PC (2.29 mmol L^{-1} cm^{-2}) processes. Therefore, in terms of the product yield, the synergistic effect of the PC and EC reductions of CO_2 on Cu_2O/Fe_2O_3 NTs-30 was thoroughly proved.

In addition, to verify the importance of material design, the PEC reduction of CO_2 on Cu_2O/Fe_2O_3 NTs-30, Cu_2O/Fe, and Fe_2O_3 NTs were carried out. The results showed that the CH_3OH yield on Cu_2O/Fe_2O_3 NTs-30 after 6 h was larger than those on Cu_2O/Fe (0.55 mmol L^{-1} cm^{-2}), Fe_2O_3 NTs (1.29 mmol L^{-1} cm^{-2}), and the addition of both the processes (1.84 mmol L^{-1} cm^{-2}). Therefore, another synergistic effect existed, i.e., the synergistic function between Cu_2O and Fe_2O_3 NTs.

Finally, the faradaic efficiency well explained the synergistic function. As shown in Figure 5d, the faradaic efficiencies of Fe_2O_3 NTs and Cu_2O/Fe for the conversion of CO_2 to CH_3OH were only ~35% and 40%, respectively. However, the faradaic efficiency of Cu_2O/Fe_2O_3 NTs-30 reached 93%. This is probably because the existence of two synergistic functions leaded to such a high faradaic efficiency.

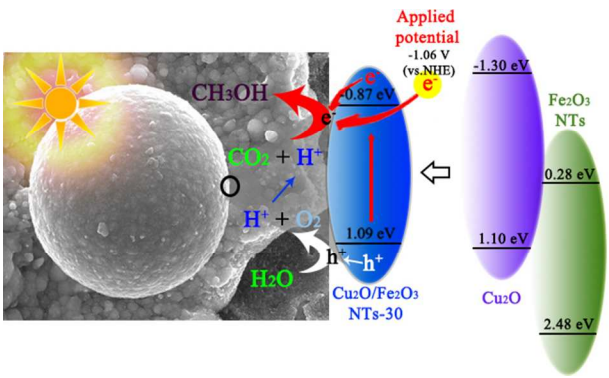

Scheme 2. Mechanism of the photoelectrocatalytic reduction of CO_2 on Cu_2O/Fe_2O_3-30 nanotubes.

According to the above analysis and discussion, the mechanism of the PEC reduction of CO_2 on Cu_2O/Fe_2O_3 NTs-30 was deduced. As shown in Scheme 2, two reactions occurred on the electrode surface under irradiation: (i) water was oxidized by the photogenerated holes to protons and oxygen because of the valence band at 1.09 eV, which was higher than the oxidation potential of H_2O/O_2 (0.82 V vs. NHE). Therefore, the as-prepared material could supply enough protons for the CO_2 reduction by the valence-band oxidation. (ii) CO_2 could be reduced to CH_3OH. On the one hand, the suitable conduction band of the as-prepared material was -0.87 eV, which was more negative than the reduction potential of CO_2/CH_3OH (-0.38 V vs. NHE). This indicated that the catalyst possessed enough PC reductive ability to reduce CO_2 to CH_3OH. On the other hand, the external potential could not only enhance the separation of electrons and holes to improve the PC reduction of CO_2, but also supplied sufficient electrons to sustain the EC reduction of CO_2. Thus, the high efficiency of the PEC synergistic reduction of CO_2 on the Cu_2O/Fe_2O_3 NTs-30 could be reasonably explained.

Experimental Section

Preparation of Catalysts

Cu_2O/Fe_2O_3 NTs were prepared by the potentiostatic electrodeposition method by depositing a Cu_2O film on the surface of Fe_2O_3 NTs. Further, the Fe_2O_3 NTs were obtained by the potentiostatic anodization method according to a previous report published by our group[23]. The electrodeposition experiments were performed under 0.5 V for 30 min (20 °C). The Fe_2O_3 NTs were the working electrode, and the titanium foil was the counter electrode. The electrolytes comprised 0.4 mol L^{-1} $CuSO_4$ and 3 mol L^{-1} lactic acid. After washing with water and ethanol and drying, the Cu_2O/Fe_2O_3 NTs were obtained. The Cu_2O/Fe was prepared by a similar potentiostatic electrodeposition method in which the working electrode was pure Fe plate, not Fe_2O_3 NTs.

Characterization

The surface morphologies of the as-prepared samples were characterized by scanning electron microscopy (SEM, Philips XL30 FEG) using an accelerated voltage of 20 kV. The particle size was tested by the nano measurer software, and the result was the mean value, the standard deviation is less than 4.66%. The crystals were characterized by XRD) (Rigaku D/MAX-rA, Japan) using a diffractometer with Cu Kα radiation, λ = 1.54184 Å in the range 2θ = 20-80° and a scan rate of 4° min^{-1}. The surface compositions were detected by XPS, ESCALAB 250, using a monochromatic X-ray source (Al Kα $h\upsilon$ = 1486.6 eV). The photochemical properties were determined by measuring the UV-visible absorbance spectra using IS19-1 combined with a single reflection internal accessory (Beijing Purkinje General Instrument Co., Ltd). The electrochemical properties were measured by CHI660D electrochemical workstation (Shanghai Chenhua Instrument Co., Ltd.).

The PEC properties were measured using a CHI660D electrochemical workstation. A SCE was used as the reference electrode; a platinum wire was used as the counter electrode; and the as-prepared materials were used as the working electrode. A 500 W xenon lamp (Solar-500, NBeT Group Corp.) with a filter ($\lambda \geq$ 420 nm, 100 mW cm^{-2}) served as the visible light source. LSV and Amperometric *i-t* curves were measured in 0.1 mol L^{-1} $KHCO_3$ with the scan rate 50 mV s^{-1}. N_2 or CO_2 was bubbled into the $KHCO_3$ solution at the rate of 40 sccm for 20 min before the experiment started. Overpotential of CO_2 reduction is equal to the D-value between the actual reduction potential and the theoretical reduction potential (CO_2/CH_3OH=-0.38 V vs. NHE).

The PEC reduction of CO_2 experiments were conducted in a double cell reactor with circulating water at the constant temperature of 25 °C. Cu_2O/Fe_2O_3 NTs, platinum slice, and SCE were used as the working electrode, counter electrode, and reference electrode, respectively. The electrode area was 2 × 2 cm^2, electrode interval was 1.0 cm, flow rate of CO_2 was 40 sccm during the entire experiment. A 500 W xenon lamp ($\lambda \geq$ 420 nm, 100 mW cm^{-2}) served as the source of visible light. The intermediates and products were detected by gas chromatography (6890-N, Agilent) using a column (2 m, inner diameter 3 mm, Parapok Q, 80-100) and flame ionization detector. The column temperature was maintained at 100 °C, while the detector temperature was maintained at 150 °C. High purity N_2 was used as the carrier gas with a flow rate of 30 sccm. All the experimental data were taken from the average of three parallel experiments.

Conclusions

In this study, Cu_2O/Fe_2O_3 NTs were prepared by the potentiostatic electrodeposition method in which Cu_2O film was deposited onto the surface of Fe_2O_3 NTs. The growth mechanism of Cu_2O/Fe_2O_3 NTs was studied in detail; the Cu_2O film showed various structures with the progress in the electrodeposition. Moreover, diverse photoelectric properties were determined for the materials with different morphologies. Among them, the material with double-layer Cu_2O spheres (Cu_2O/Fe_2O_3NTs-30) showed excellent PEC properties with a suitable energy band gap (1.96 eV) and smallest overpotential (180 mV). The morphology and composition of Cu_2O/Fe_2O_3NTs-30 were determined by the XRD and XPS analyses. Furthermore, Cu_2O/Fe_2O_3NTs-30 showed two types of synergism in the PEC reduction of CO_2: (i) between electrocatalysis and photocatalysis and (ii) between Cu_2O and Fe_2O_3NTs. The faradaic efficiency and methanol yield reached 93% and 4.94 mmol L^{-1} cm^{-2} after 6 h, respectively. The outstanding performance of Cu_2O/Fe_2O_3NTs-30 for the PEC reduction of CO_2 was well confirmed. Finally, the mechanism for the reduction CO_2 by Cu_2O/Fe_2O_3NTs-30 was elucidated in detail.

Acknowledgements

This research was supported by the National Natural Science Foundation of China (Grant No. 21203114), Key Projects in the National Science and Technology Pillar Program during the Twelfth Five-year Plan Period (Grant No. 2011BAD11B01), and Promotive Research Fund for Excellent Young and Middle-aged Scientists of Shandong Province (Grant No. BS2012NJ008) and Science and Technology Development Planning of Shandong province (Grant No. 2013GZX20109). We are grateful to the foundation supported by Shandong Jingbo Holdings Corporation.

Notes and references

** 61 Daizong Road, Tai'an, People's Republic of China. Tel: 86-0538-8249017.*
E-mail: chem_carbon@outlook.com; pqli@sdau.edu.cn.

† Electronic Supplementary Information (ESI) available: [details of any supplementary information available should be included here]. See DOI: 10.1039/b000000x/

1 M. E. Berndt, D. E. Allen and W. E. Seyfried, *Geol.* **1996**, *24*, 351-354.
2 X. Guo, D. Mao, S. Wang, G. Wu and G. Lu, *Catal. Commun.* **2009**, *10*, 1661-1664.
3 C.-C. Lo, C.-H. Hung, C.-S. Yuan and J.-F. Wu, *Sol. Energy Mater. Sol. Cells.* **2007**, *91*, 1765-1774.
4 S. S. Tan, L. Zou and E. Hu, *Catal. Today.* **2008**, *131*, 125-129.
5 J. Ettedgui, Y. Diskin-Posner, L. Weiner and R. Neumann, *J. Am. Chem. Soc.* **2010**, *133*, 188-190.
6 Y. Hori, A. Murata and R. Takahashi, *J. Chem. Soc., Faraday Trans. 1*, **1989**, *85*, 2309-2326.
7 S. Kaneco, H. Katsumata, T. Suzuki and K. Ohta, *Electrochim. acta*, **2006**, *51*, 3316-3321.
8 N. V. Rees and R. G. Compton, *Energy Environ. Sci.*, **2011**, *4*, 403-408.
9 Y. Hori, I. Takahashi, O. Koga and N. Hoshi, *J. Phys. Chem. B.* **2002**, *106*, 15-17.
10 Arrigo, R.; Schuster, M. E.; Wrabetz, S.; Girgsdies, F.; Tessonnier, J. P.; Centi, G.; Perathoner, S.; Su, D. S.; Schlögl, R. *ChemSusChem.* **2012**, *5*, 577-586.
11 Y. Hori, H. Wakebe, T. Tsukamoto and O. Koga, *Electrochim. acta*, **1994**, *39*, 1833-1839.
12 J. Augustynski, P. Kedzierzawski and B. Jermann, *Stud. Surf. Sci. Catal.* **1998**, *114*, 107-116.
13 M. Halmann, *Nat.* **1978**, *275*, 2.
14 J. Gu, A. Wuttig, J. W. Krizan, Y. Hu, Z. M. Detweiler, R. J. Cava and A. B. Bocarsly, *J. Phys. Chem. C.* **2013**, *117*, 12415-12422.
15 E. E. Barton, D. M. Rampulla and A. B. Bocarsly, *Am. Chem. Soc.* **2008**, *130*, 6342-6344.
16 B. Kumar, M. Llorente, J. Froehlich, T. Dang, A. Sathrum and C. P. Kubiak, *Annu. Rev. Phys. Chem.* **2012**, *63*, 541-569.
17 P. Li, H. Hu, J. Xu, H. Jing, H. Peng, J. Lu, C. Wu and S. Ai, *Appl. Catal. B: Environ.* **2013**, *147*, 912-919
18 Y.-M. Lin, P. R. Abel, A. Heller and C. B. Mullins, *J. Phys. Chem. Lett.* **2011**, *2*, 2885-2891.
19 A. Kleiman-Shwarsctein, M. N. Huda, A. Walsh, Y. Yan, G. D. Stucky, Y.-S. Hu, M. M. Al-Jassim and E. W. McFarland, *Chem. Mater.* **2009**, *22*, 510-517.
20 G. Liu, Q. Deng, H. Wang, D. H. Ng, M. Kong, W. Cai and G. Wang, *J. Mater. Chem.* **2012**, *22*, 9704-9713.
21 D. K. Bora, A. Braun, R. Erni, G. Fortunato, T. Graule and E. C. Constable, *Chem. Mater.* **2011**, *23*, 2051-2061.
22 A. Mao, K. Shin, J. K. Kim, D. H. Wang, G. Y. Han and J. H. Park, *ACS Appl. Mater. Interfaces*. **2011**, *3*, 1852-1858.
23 P. Li, H. Wang, J. Xu, H. Jing, J. Zhang, H. Han and F. Lu, *Nanoscale*, **2013**, *5*, 11748-11754.
24 T.-Y. Chang, R.-M. Liang, P.-W. Wu, J.-Y. Chen and Y.-C. Hsieh, *Mater. Lett.* **2009**, *63*, 1001-1003.
25 J. Bugayong and G. L. Griffin, *ECS Trans*, **2013**,*58*, 81-89.
26 X. Wen, S. Wang, Y. Ding, Z. L. Wang and S. Yang, *J. Phys. Chem. B.* **2005**, *109*, 215-220.
27 Z. Zhang, M. F. Hossain and T. Takahashi, *Appl. Catal. B: Environ.* **2010**, *95*, 423-429.
28 W. Z. Wang, G. Wang, X. S. Wang, Y. Zhan, Y. Liu and C. L. Zheng, *Adv. Mater.* **2002**, *14*, 67-69.
29 Y. Zhu, W. Y. Wang, M. W. Guo, G. Li, H. J. Lu, *Inorg. Chem. Comm.* **2011**, *14*, 1432-1435.
30 M. Muhler, R. Schlögl and G. Ertl, *J. Catal.* **1992**, *138*, 413-444.
31 L. Larina, O. Shevaleevskiy and B. T. Ahn, *Energy Environ. Sci.* **2011**, *4*, 1480-1486.